AGU PUBLICATIONS

Geophysical Research Letters

RESEARCH LETTER
10.1002/2015GL065218

Special Section:
First Results from the MAVEN Mission to Mars

MHD model results of solar wind interaction with Mars and comparison with MAVEN plasma observations

Y. J. Ma[1], C. T. Russell[1], X. Fang[2], Y. Dong[2], A. F. Nagy[3], G. Toth[3], J. S. Halekas[4], J. E. P. Connerney[5], J. R. Espley[5], P. R. Mahaffy[5], M. Benna[5], J. P. McFadden[6], D. L. Mitchell[6], and B. M. Jakosky[2]

[1]Department of Earth Planetary and Space Sciences, UCLA, Los Angeles, California, USA, [2]Laboratory for Atmospheric and Space Physics, University of Colorado Boulder, Boulder, Colorado, USA, [3]Department of Atmospheric, Oceanic and Space Sciences, University of Michigan, Ann Arbor, Michigan, USA, [4]Department of Physics and Astronomy, University of Iowa, Iowa City, Iowa, USA, [5]NASA Goddard Space Flight Center, Greenbelt, Maryland, USA, [6]Space Sciences Laboratory, University of California, Berkeley, California, USA

Abstract The Mars Atmosphere and Volatile EvolutioN mission (MAVEN), launched on 18 November 2013, is now in its primary science phase, orbiting Mars with a 4.5 h period. In this study, we use a time-dependent MHD model to interpret plasma observations made by MAVEN particle and field instruments. Detailed comparisons between the model and the relevant plasma observations from MAVEN are presented for an entire Mars rotation under relatively quiet solar wind conditions. Through comparison along MAVEN orbits, we find that the time-dependent multispecies single-fluid MHD model is able to reproduce the main features of the plasma environment around Mars. Using the model results, we find that photoionization beyond the terminator is the dominant ion source as compared with day-night transport in maintaining the nightside ionosphere. Model results also show that both the time-varying solar wind conditions and the continuously rotating crustal field work together to control the ion escape variation with time.

Key Points:
- A time-dependent MHD model is used to interpret plasma observations made by MAVEN
- Photoionization beyond the terminator is the dominant ion source for the nightside ionosphere
- Both solar wind conditions and the rotating crustal field control the ion escape from Mars

Supporting Information:
- Suppoting Information S1
- Figure S1
- Figure S2

Correspondence to:
Y. J. Ma,
yingjuan@igpp.ucla.edu

Citation:
Ma, Y. J., et al. (2015), MHD model results of solar wind interaction with Mars and comparison with MAVEN plasma observations, *Geophys. Res. Lett.*, *42*, doi:10.1002/2015GL065218.

Received 7 JUL 2015
Accepted 21 AUG 2015

1. Introduction

The plasma interaction around Mars is more complex than that around Venus due to the presence of crustal field anomalies on Mars. The localized crustal magnetic anomalies [*Acuna et al*., 1999; *Connerney et al*., 2001] rotate constantly with the planet, affecting the magnetic field configuration and its interaction with the solar wind. The daily variation of the crustal field configuration is also modulated by different Mars seasons as the tilt angle of the rotation axis relative to the Sun changes.

Numerous global models have been applied to Mars (see reviews of *Nagy et al*., 2004; *Ledvina et al*., 2008; *Brain et al*., 2010; *Kallio et al*., 2011 and references therein) to understand the plasma environment of Mars. Those earlier numerical studies were usually restricted to stationary solar wind situations and neglected the rotation of the crustal anomalies. *Y. Ma et al*. [2014] first included the temporal variation of the rotating crustal magnetic field into a global interaction model of Mars using a realistic orientation of the planet's rotation axis. The model results were found to be in excellent agreement with Mars Global Surveyor (MGS) magnetometer observations. The time-dependent simulation also showed significant fluctuations in the ion loss rates driven by the rotation of the nonuniform crustal anomalies [*Y. Ma et al*. 2014]. Further analysis of the model results by *Fang and Ma* [2014] suggests that the ion loss rates are controlled by the crustal magnetic pressure in both the subsolar regime and the terminator region.

The NASA Mars Atmosphere and Volatile EvolutioN mission (MAVEN) [*Jakosky et al*., 2015], launched on 18 November 2013, is now in its primary science phase, orbiting Mars with a 4.5 h period. The MAVEN mission carries on board a complete set of plasma instruments to provide measurement of the solar wind input and the plasma environment near Mars, making it ideal to further validate the time-dependent MHD model. Additionally, MAVEN is in an eccentric orbit with an apoapsis around 6400 km altitude and periapsis normally at 150 km altitude except during several deep dips. For most of the orbits, MAVEN would pass through different plasma regions, which include the solar wind, magnetosheath, the induced magnetosphere, and the ionosphere. So comparison with MAVEN serves as a comprehensive evaluation for the general performance of the model. In this study, we present detailed comparison of the time-dependent MHD model results with relevant MAVEN plasma observations along the spacecraft orbit under relatively quiet solar wind conditions. The model is briefly described in section 2. Solar wind input of the model

and a brief description of MAVEN orbit are presented in section 3. Detailed data and model comparison is shown in section 4. A summary is given in section 5.

2. Model Description

A multispecies single fluid MHD model of Mars is used for the time-dependent calculation employing the University of Michigan BATS-R-US code [*Powell et al*., 1999; *Toth et al*., 2012]. The MHD model has been described in detail by *Y. Ma et al*. [2014]. The model solves four continuity equations to track the mass densities of the proton and three major ions in the Martian ionosphere: O_2^+, O+, and CO_2^+. All ion species share the same velocity and temperature. The Mars-solar wind interaction is self-consistently calculated in the model by including the effects of the crustal anomalies, ion-neutral collisions, and major chemical reactions. The neutral densities of CO_2, O, and H are assumed to be spherically symmetric, and the altitude profiles and EUV strength are the same as used for the solar minimum condition in *Ma et al*. [2004]. The crustal field is calculated based on the 60-order spherical harmonics from *Arkani-Hamed* [2001].

In the earlier versions of our model, the optical depth effect is included by a cosine approximation for different solar zenith angles (SZA) [*Y. Ma et al*., 2004, 2014; *Y. J. Ma et al*., 2014]. Such a method would provide no photionization at the nightside (SZA $>$ 90°). In the model, the nightside ionosphere can only be maintained through electron impact ionization and day-night transport driven primarily by pressure gradient. Strictly speaking, some regions beyond the terminator are still in sunlight [*Lillis et al*., 2009], even though the solar EUV fluxes would be absorbed considerably by the atmosphere depending on altitude and SZA. In order to include photoionization effects beyond the terminator at SZA larger than 90°, we adopt in this study, the Chapman function [*Smith and Smith*, 1972; *Huestis*, 2001]. We find that the Chapman function method significantly improves the agreement with the plasma density observations around the terminator, as will be discussed in more detail later.

The model calculations are performed in the Mars-centered Solar Orbital (MSO) coordinate system: the *X* axis points from Mars to the Sun, the *Y* axis points antiparallel to Mars' orbital velocity, and the *Z* axis completes the right-handed coordinate system. In order to compare with MAVEN observations, the rotation axis of Mars is chosen to be (−0.4, −0.15, 0.905), corresponding to the value in the middle of a selected day on 10 December 2014. At the beginning of this day, the subsolar location is 132°E and 23.5°S. The season on Mars during that time was southern summer. The rotation period relative to the Sun was 24.67 h, slightly longer than the sidereal day.

3. Solar Wind Input of the Model and MAVEN Orbit

We simulate an entire day of plasma interaction on 10 December 2014 when the solar wind condition was relatively quiet, in order to minimize the variation of the Martian plasma environment caused by changes in the solar wind. The average solar wind condition from MAVEN on 10 December 2014 was: $n_{SW} = 3.6\ cm^{-3}$; $U_{SW} = 400$ km/s, $T_P = 3.0 \times 10^5$ K; and $B = (-0.9, 2.3, 0.0)$ nT. This corresponds to a dynamic pressure of 1.0 nPa and magnetosonic Mach number of 6.2. While the solar wind flow speed was relatively steady during the selected time period with less than 10% variation, the solar wind density and interplanetary magnetic field (IMF) showed quite large variations (more than 50%). To take into account the solar wind variation in the model, we used a time-varying solar wind input to the model. We first determine the time intervals when MAVEN was in the solar wind. During those time intervals, the input solar wind conditions are specified by 2 min average MAVEN measurements (see Figure 3, grey regions). Specifically, the time series of the solar wind density, velocity, and ion temperature are calculated based on Solar Wind Ion Analyzer (SWIA) [*Halekas et al*., 2013]. The solar wind electron temperature is estimated using Solar Wind Electron Analyzer (SWEA). The IMF is averaged from magnetometer (MAG) observations [*Connerney et al*., 2015]. A few minutes of the data before/after the inbound/outbound BS crossing were removed to avoid the influence from the foreshock. Measured solar wind values were connected with a straight line to fill the gap.

Figure 1 shows a three-dimensional view of the MAVEN orbit on 10 December, from 16 UT to 20:30 UT. The rest of the orbits on the day have very similar geometry. The color on the sphere corresponds to the crustal field magnitude at 10 December, 18 UT, when the strong crustal anomalies were facing toward the Sun. The color on the orbit shows the altitude of the spacecraft, which is between 150 km to 6400 km. As can be seen

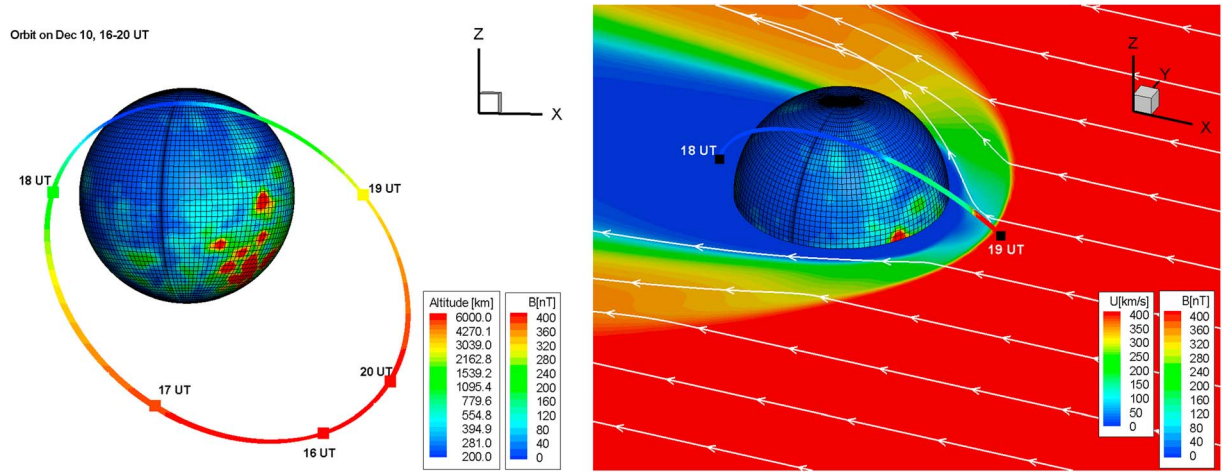

Figure 1. Three-dimensional view of MAVEN Trajectory from 16 UT to 20 UT on 10 December 2014. The color on the sphere corresponds to the crustal field magnitude at 18 UT on 10 December. (left) The color on the orbit shows the altitude. (right) MAVEN orbit in context of the MHD model results, the color on the orbit, and in the ecliptic plane shows the flow speed from the MHD model.

from the figure, the MAVEN orbit was close to the meridional plane, with the north part of the orbit slightly tilted toward the dawnside. The spacecraft passed by the center of the downstream plasma wake region near 18 UT, 20 min before it flew by the periapsis near the north polar region. Note that the position of the MAVEN trajectory is slightly enlarged by a small factor of 1.006 (= 3396.0/3376.0). The small adjustment is made to get the right altitude near periapsis, considering the fact that the polar radius of Mars is 3376 km, about 20 km less than the equatorial radius, while the model assumes a spherical body using the equatorial radius.

4. MHD Model Results and Comparison With MAVEN Observations

Figure 2 shows model and observation comparison along the MAVEN orbit from 2:20 UT to 5:40 UT. The Figure 2a shows the trajectory information. The inbound pass occurred in the nightside region with SZA $>$ 90°, while the outbound pass occurred mostly in the dayside region. Figures 2b–2d compare the MHD model results with SWIA, STATIC (the Superthermal and Thermal Ion Composition instrument) [*McFadden et al.*, 2015], and MAG observations along the MAVEN orbit. At 2:20 UT, MAVEN was located near apoapsis, about 2.8 Mars radii away from the center of the planet, and was observed to be situated in the upstream solar wind. The magnetic field was mainly along the positive *Y* direction in the solar wind. The inbound bow shock crossing occurred at around 2:55 UT as marked by the vertical dashed line according to plasma observations. The shock position predicted by the MHD model is almost identical to the location of the observed boundary. Across the shock, both model and observation show sharp increase in proton density, significant slowdown of the flow speed, rotation of the plasma flow vector, and a sharp increase of the magnetic field.

Inside the bow shock is the magnetosheath region. MAVEN observed strong fluctuations in the magnetic field and plasma flow. Both the wave activity ahead of the shock and waves inside the magnetosheath region could not be reproduced by the MHD model due to the fluid approximation. However, the flow vector and magnetic field strength predicted by the model follow closely with the averaged properties of the plasma in the magnetosheath region. The observed magnetic field directions (see supporting information of the paper) showed complex signatures. And there was a B_Y reversal around 3:24 UT, likely due to the direction change of the interplanetary magnetic field, which could not be given back by the model since we assumed constant solar wind properties there.

Across the induced magnetosphere boundary (IMB), MAVEN moved into the magnetotail region. Plasma conditions changed from the shocked solar wind to planetary ion dominated region, where the plasma was much slower and the magnetic field pressure was dominant over the dynamic pressure. In the magnetotail lobe region, the direction of magnetic field was steady and mainly pointing toward the planet. The current sheet (CS) crossing occurred at 4:15 UT, when magnetic field reversed its orientation suddenly to pointing

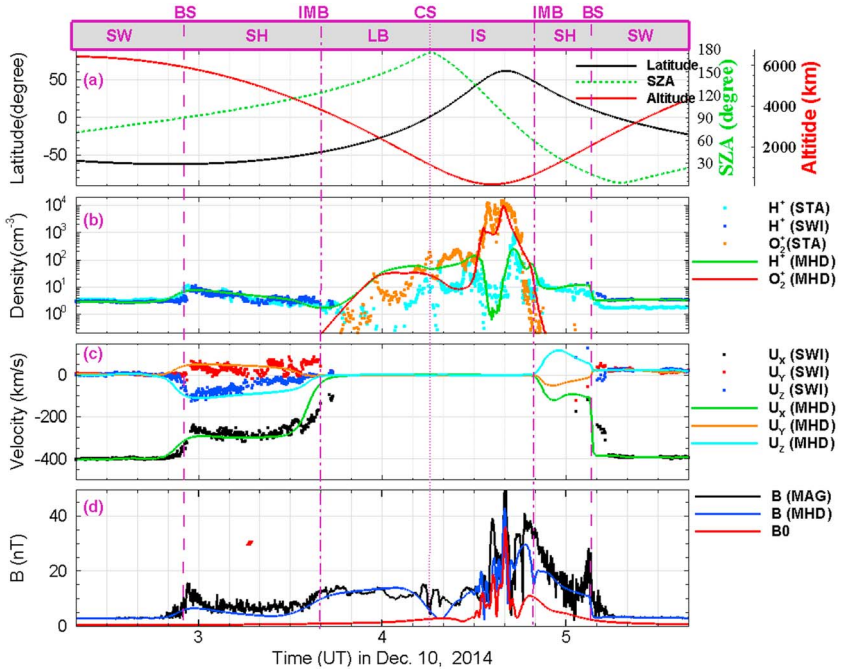

Figure 2. Model and observation comparison along the orbit of MAVEN. (a) The satellite latitude, solar zenith angle, and altitude along the trajectory. (b–d) Comparison of the plasma density, velocity, and magnetic field strength with relevant plasma observations along the MAVEN orbit. The vertical lines mark the locations of different plasma boundaries that MAVEN passed: bow shock (BS, dashed lines), induced magnetosphere boundary (IMB, dash-dotted lines), and current sheet (CS, dotted line). Different plasma regions are also indicated at the top of the figure: solar wind (SW), magnetosheath (SH), magnetotail lobe (LB), and ionosphere (IS).

away from Mars (see supporting information of the paper). The predicted time for CS crossing by the model is about 3 min later than in the observation and is not as sharp as observed. After the CS crossing, as MAVEN moved closer to the planet, it entered into the nightside ionosphere. The exact location of the outer boundary of the ionosphere is hard to determine in the case, due to the large variation of the ion densities as indicated from STATIC measurements. Significant fluctuations in the nightside ionosphere were also observed by the Radio Science experiment and Mars Advanced Radar for Subsurface and Ionospheric Sounding radar sounder on board of Mars express [*Withers et al*., 2012; *Diéval et al*., 2014]. MAVEN then passed through periapsis (~150 km altitude) at around 4:35 UT and moved into the dayside ionosphere. Both STATIC and the MHD model show that O_2^+ is the dominant ion in the ionosphere. Besides STATIC, MAVEN carries another instrument that is capable of measuring ion densities in the ionosphere, the Neutral Gas and Ion Mass Spectrometer (NGIMS) [*Mahaffy et al*., 2014]. However, NGIMS was in neutral mode during this orbit, thus did not make ion density measurements. A detailed comparison of the plasma densities predicted by the model and NGIMS and STATIC observations will be discussed in more detail later on another orbit. As MAVEN moved farther away from the planet, after outbound crossings of the IMB and the BS, it entered the solar wind after 5:10 UT.

The crustal field near periapsis is quite strong according to the crustal field model of *Arkani-Hamed* [2001], with a peak value of 35 nT, as shown by the red line in Figure 2d. This is a comparable magnitude to the induced magnetic field. The highest peak of the magnetic field around 4:40 UT is 52 nT. Both the peak time and value are well captured by the model. There were also a few observed peaks shortly before and after the periapsis but were not reproduced by the MHD model. The magnetic field direction near peripasis showed very complicated patterns due to strong crustal field and possibly changes in the solar wind.

The MHD model results not only match well with the plasma observations from SWIA and MAG during this particular orbit shown in Figure 2 but also agree well with the observations for the entire day of 10 December 2014, as shown in Figure 3. Second to seventh panels show the comparisons between the model and MAVEN observations where the observations are in black. To quantify the comparison, we calculated the

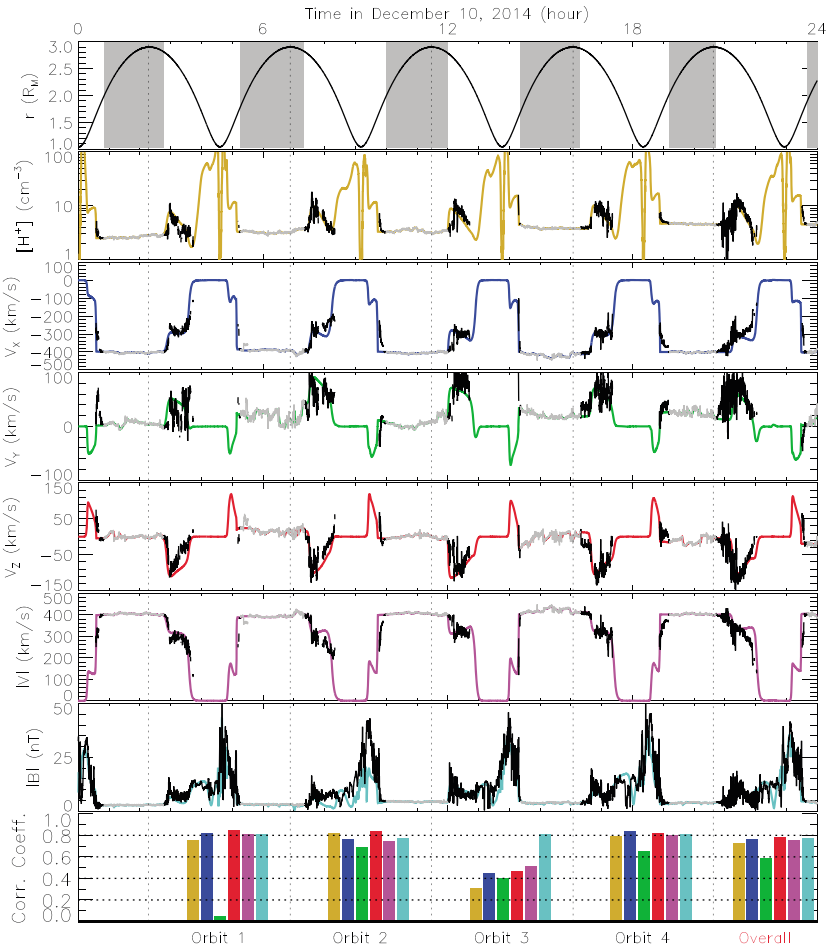

Figure 3. Comparison of the MHD model results with the MAVEN observations along the spacecraft orbit on 10 December 2014. The first panel shows the radial distance of the spacecraft from the Mars center. The grey regions mark the time periods when the input solar wind conditions are specified by MAVEN measurements. Second to seventh panels show the comparisons between the model and MAVEN observations where the observations are in black. The color bars in the eighth panel are the correlation coefficients for H+ (golden), V_X (blue) V_Y (green), V_Z (red), V (purple), and B (light blue), respectively, for each corresponding orbit as separated by the vertical dashed lines.

correlation coefficients for each of the orbits during the day for different plasma parameters as indicated by the color bars in the eighth panel of the figure. The separation of the orbits is by the apoapsis as marked by the vertical dashed lines. The correlation coefficient is defined as $r = \frac{\sum_{i=1}^{i=n}(x_i-\overline{x})(y_i-\overline{y})}{\sqrt{\sum_{i=1}^{i=n}(x_i-\overline{x})^2}\sqrt{\sum_{i=1}^{i=n}(y_i-\overline{y})^2}}$, where $\overline{x}$ and $\overline{y}$ are the mean values of x and y variables. The correlation coefficients in general are fairly high (>0.80 for most orbits/parameters); but they do vary significantly from orbit to orbit, especially for the UY component. The model-calculated magnetic field strength correlates well with observed field strength. But the calculated components of the magnetic field do not have good correlation with the observed magnetic field vectors (see supporting information of the paper), much lower than the correlation coefficients that we obtained in comparison with the MGS observations [*Y. Ma et al.*, 2014]. This could be due to two reasons: (1) even though we considered the variation of the IMF change when MAVEN is in the solar wind, we do not know how the IMF changes when MAVEN is inside the bow shock. Thus, some of the discrepancy could be due to changes of the IMF. (2) The crustal field model used in the MHD model is based on MGS observations (mostly at 400 km altitude); thus, its prediction at low altitudes might not be accurate.

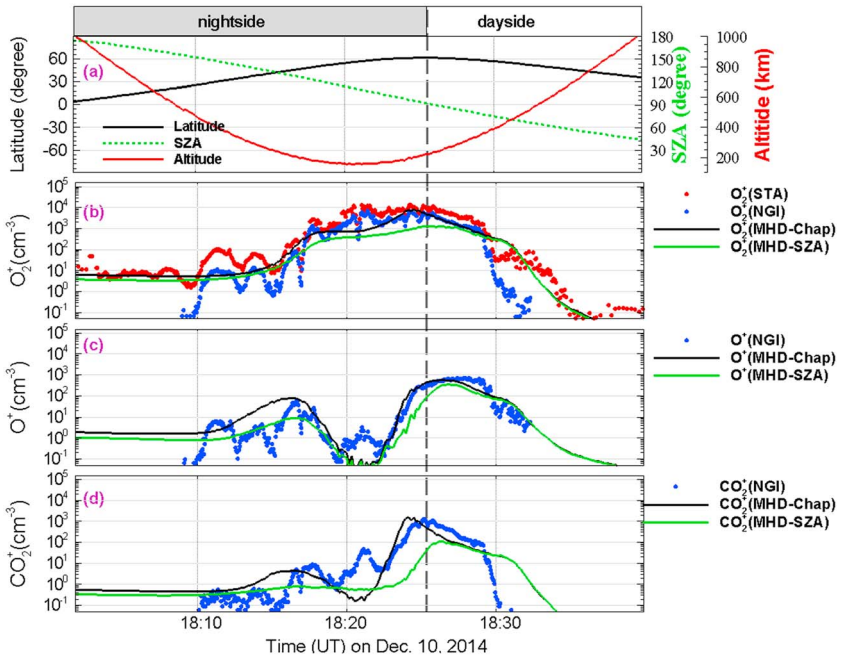

Figure 4. Comparison of different ion density results obtained from two different MHD models (SZA and Chapman) and two independent in situ measurements (STATIC and NGIMS) between 18:00 UT to 18:40 UT. (a) The ephemeris information, in the same form as Figure 2a. (b–d) Comparisons for O_2^+, O^+, and CO_2^+, respectively. The STATIC data are plotted in red, NGIMS measurements are in blue, and MHD model results for two different cases are plotted in black (Chapman) and green (SZA). The dashed vertical line marks the times when MAVEN passed the terminator.

Comparisons of planetary heavy ion densities from the MHD model and MAVEN observations are shown in Figure 4, around the periapsis of the fourth orbit of the day. Two model results are shown in this figure: the green lines are results when the photoionization rates are estimated using a simplified cosine approximation of SZA and the black curves correspond to the model results when the photoionization rates are calculated using the Chapman function. In most of the plasma regions, the model results of the two cases are very close to each other considering the plasma boundary locations and the plasma properties. An exception is in the deep ionosphere at relatively high SZA. Significant differences are present between the two cases when SZA is greater than 75°. As the Chapman function provides a more accurate description of the absorption of the solar flux at high SZA, the model-observation agreement near the terminator is significantly improved.

Comparison of the two MHD model runs also sheds light on how important the day-night transport flow is in maintaining the nightside ionosphere. In the MHD-SZA case, the photoionization rates were set to zero for SZA $>$ 90. The only two sources of the nightside ionosphere included in the model are transport and electron impact ionization. While in the MHD-Chapman case, photoionization beyond the terminator is also included in the calculation. And the good agreement between MHD-Chapman and NGIMS observation clearly demonstrated that at altitude range from 150 km to 400 km, the most important ion source for the nightside ionosphere where SZA $<$ 115° is photoionization. Only in the deep ionosphere, when the EUV flux is completely absent, the electron impact ionization and transport are the major ion sources. The relative importance of the two depends on the solar wind conditions. When the electron impact ionization in the model is turned off, we found in most regions a ~20% decrease in nightside ion densities, suggesting that under nominal conditions, transport is the dominant process in maintaining the nightside ionosphere. However, keep in mind that the electron impact that included in the model is simply based on the thermal population of the electrons and the ionization frequency is calculated based on electron temperature [*Cravens et al.*, 1987]. Potential effect from suprathermal electrons is currently neglected in the model. The localized peak around 18:21 UT in both NGMIS and STATIC data occurred around 160 km altitude beyond the terminator. It is probably due to some transient ionization sources such as Ablation by meteoroid influx [*Withers*, 2009], transient SEP [*Leblanc et al.*, 2002], or gamma ray burst events [*Espley et al.*, 2008] that were not included in the MHD model.

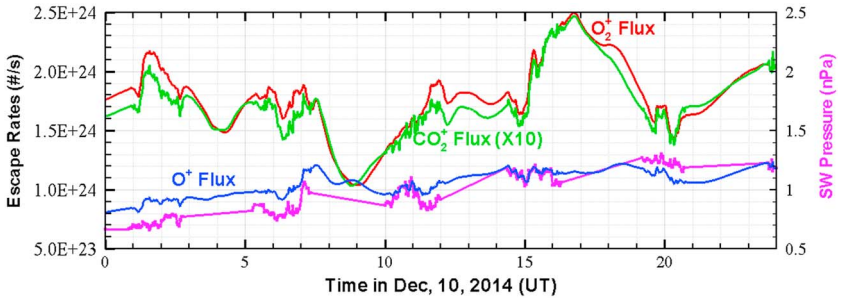

Figure 5. Variation of the modeled escape rates with time. The solid lines are integrated loss rates for O^+ (blue), O_2^+ (red), and CO_2^+ (green, increased by a factor of 10 for better comparison). The purple line shows solar wind dynamic pressure calculated based on the time-varying solar wind input of the model.

Both the observation and model results show that O_2^+ is the dominant ion in the ionosphere below ~ 300 km altitude, consistent with Viking observations and previous model predictions [*Hanson et al*., 1977; *Chen et al*., 1978; *Fox*, 2004]. Also, we find in general good agreement with MAVEN observations for O_2^+ when SZA $< 105°$. Specifically, the MHD model agrees well with NGIMS observations of O_2^+ below 350 km altitudes. Above this altitude, the model shows a closer agreement with STATIC data. This is because at high altitudes, plasma flow speed is generally higher, and NGIMS does not provide a complete measurement of the ion distribution, due to its narrow aperture, so the STATIC measurement is more reliable. Both STATIC and NIGIMS observed wave-like structures in the ion density in the deep nightside ionosphere, which are not reproduced by the model. This is likely due to strong perturbations of the neutral density in the nightside region, which were observed by NGIMS but were not taken into account in the current MHD model. According to NGIMS observations, O^+ becomes the major ion above 300 km altitude, while the MHD model predicts that O^+ density never overtakes O_2^+. The discrepancy is likely caused by the neutral profile that used in the model was still based on Viking observation.

Figure 5 shows globally integrated planetary ion loss rates during the day. The escaping plasma is dominated by O_2^+ for the majority of the time. The averaged total ion escape rate is about $2.5 \times 10^{24}\,s^{-1}$, in the same range as the average heavy ion escape rate estimated from Mars Express observations near solar minimum condition [*Lundin et al*., 2013]. The O_2^+ escape rate reaches a minimum of $1.0 \times 10^{24}\,s^{-1}$ around 9 UT and a maximum of $2.5 \times 10^{24}\,s^{-1}$ around 16:30 UT. The loss rate of O^+ show a simultaneous response to changes of the solar wind dynamic pressure, while the loss rates of the two heavy ions (O_2^+ and CO_2^+) do not show direct dependence on the solar wind conditions. The variation is larger here as compared with the event on 16 May 2005 event investigated by *Y. Ma et al*. [2014]. There are two reasons. First, the larger variation could come from the seasonal effect. As mentioned earlier in the paper, the season for the current study is southern summer; thus, we expect the crustal field to have a stronger modulation of the total escape rates. Second, the upstream solar wind dynamic pressure also varies during the time period. As shown by the purple line in the figure, the solar wind dynamic pressure was about 0.7 nPa at the beginning of the day and increased to 1.3 nPa near the end of the day. And it is expected that both the time-varying solar wind conditions [*Y. J. Ma et al*., 2014] and the continuously rotating crustal field [*Fang et al*., 2010; *Fang and Ma*, 2014; *Y. Ma et al*., 2014] work together to control the ion escape variation with time.

5. Summary and Conclusions

Through comparison with relevant MAVEN plasma observations, we find that in general, the time-dependent multispecies MHD model reproduces well the plasma interaction process around Mars. The bow shock location and plasma conditions inside the magnetosheath region from the model agree well with SWIA data. The ion density profiles predicted by the model agree well with both NGIMS and STATIC measurements. We also find that there are some discrepancies between the MHD and the observed magnetic field vectors in the magnetic pile up region most probably due to variations of the IMF and the uncertainty in the crustal field model. Using the model results, we find that photoionization beyond the terminator is the dominant ion source as compared with day-night transport in maintaining the

nightside ionosphere. Model results also show that both the time-varying solar wind conditions and the continuously rotating crustal field work together to control the ion escape variation with time. To improve the fit, the model needs to update the neutral density profiles based on MAVEN observations, and photoionization rates from the measured solar EUV spectra.

Acknowledgments

The work presented here was supported by NASA grants NNX13AO31G, NNG06GF31G, NNH1OCCO4C, and NNX11AN38G, and NSF grant AST-0908472. Resources supporting this work were provided by the NASA High-End Computing (HEC) Program through the NASA Advanced Supercomputing (NAS) Division at Ames Research Center. The MAVEN observational data used in the study were obtained from the NASA Planetary Data System (PDS). The Space Weather Modeling Framework that contains the BATS-R-US code used in this study is publicly available from http://csem.engin.umich.edu/tools/swmf". For distribution of the model results used in this study, please contact the corresponding author.

The Editor thanks Andrea Opitz and an anonymous reviewer for their assistance in evaluating this paper.

References

Acuna, M. H., et al. (1999), Global distribution of crustal magnetization discovered by the Mars Global Surveyor MAG/ER Experiment, *Science*, *284*, 790–793.

Arkani-Hamed, J. (2001), A 50-degree spherical harmonic model of the magnetic field of Mars, *J. Geophys. Res.*, *106*, 23,197–23,208, doi:10.1029/2000JE001365.

Brain, D. A., et al. (2010), A comparison of global models for the solar wind interaction with Mars, *Icarus*, *206*(1), 139–151, doi:10.1016/j.icarus.2009.06.030.

Chen, R. H., T. E. Cravens, and A. F. Nagy (1978), The Martian ionosphere in light of the Viking observations, *J. Geophys. Res.*, *83*, 3871–3876, doi:10.1029/JA083iA08p03871.

Connerney, J. E. P., M. H. Acuña, P. J. Wasilewski, G. Kletetschka, N. F. Ness, H. Rème, R. P. Lin, and D. L. Mitchell (2001), The global magnetic field of Mars and implications for crustal evolution, *Geophys. Res. Lett.*, *28*(21), 4015–4018, doi:10.1029/2001GL013619.

Connerney, J. E. P., J. R. Espley, P. Lawton, S. Murphy, J. Odom, R. Oliversen, and D. Sheppard (2015), The maven magnetic field investigation, *Space Sci. Rev.*, 1–35, doi:10.1007/s11214-015-0169-4.

Cravens, T. E., J. U. Kozyra, A. F. Nagy, T. I. Gombosi, and M. Kurtz (1987), Electron impact ionization in the vicinity of comets, *J. Geophys. Res.*, *92*(A7), 7341–7353, doi:10.1029/JA092iA07p07341.

Diéval, C., D. D. Morgan, F. Němec, and D. A. Gurnett (2014), MARSIS observations of the Martian nightside ionosphere dependence on solar wind conditions, *J. Geophys. Res. Space Physics*, *119*, 4077–4093, doi:10.1002/2014JA019788.

Espley, J. R., J. E. P. Connerney, and R. J. Lillis (2008), Effects of high energy astrophysical events on the Martian atmosphere, in *Third International Conference on the Mars Atmosphere: Modeling and Observations*, *LPI Contrib.*, vol. 1447, p. 9110, Williamsburg, Va.

Fang, X., and Y. Ma (2014), Time variation of Mars atmospheric loss in response to continuous rotation of the crustal magnetic field, Abstract P54A-07 presented at 2014 Fall Meeting, AGU, San Francisco, Calif., 15–19 Dec.

Fang, X., M. W. Liemohn, A. F. Nagy, J. Luhmann, and Y. Ma (2010), On the effect of the martian crustal magnetic field on atmospheric erosion, *Icarus*, *206*, 130–138, doi:10.1016/j.icarus.2009.01.012.

Fox, J. L. (2004), Advances in the aeronomy of Venus and Mars, *Adv. Space Res.*, *33*, 132–139.

Halekas, J., E. Taylor, G. Dalton, G. Johnson, D. Curtis, J. McFadden, D. Mitchell, R. Lin, and B. Jakosky (2013), The solar wind ion analyzer for MAVEN, *Space Sci. Rev.*, 1–27, doi:10.1007/s11214-013-0029-z.

Hanson, W. B., S. Sanatani, and D. R. Zuccaro (1977), The Martian ionosphere as observed by the Viking retarding potential analyzers, *J. Geophys. Res.*, *82*, 4351–4363, doi:10.1029/JS082i028p04351.

Huestis, D. L. (2001), Accurate evaluation of the Chapman function for atmospheric attenuation, *J. Quant. Spectros. Radiat. Transfer*, *69*(6), 709–721.

Jakosky, B., et al. (2015), The Mars atmosphere and volatile evolution (MAVEN) mission, *Space Sci. Rev.*, 1–46, doi:10.1007/s11214-015-0139-x.

Kallio, E., J.-Y. Chaufray, R. Modolo, D. Snowden, and R. Winglee (2011), Modeling of Venus, Mars, and Titan, *Space Sci. Rev.*, *162*(1–4), 267–307, doi:10.1007/s11214-011-9814-8.

Leblanc, F., J. G. Luhmann, R. E. Johnson, and E. Chassefiere (2002), Some expected impacts of a solar energetic particle event at Mars, *J. Geophys. Res.*, *107*(A5), 1058, doi:10.1029/2001JA900178.

Ledvina, S. A., Y.-J. Ma, and E. Kallio (2008), Modeling and simulating flowing plasmas and related phenomena, *Space Sci. Rev.*, *139*, 143–189, doi:10.1007/s11214-008-9384-6.

Lillis, R. J., M. O. Fillingim, L. M. Peticolas, D. A. Brain, R. P. Lin, and S. W. Bougher (2009), Nightside ionosphere of Mars: Modeling the effects of crustal magnetic fields and electron pitch angle distributions on electron impact ionization, *J. Geophys. Res.*, *114*, E11009, doi:10.1029/2009JE003379.

Lundin, R., S. Barabash, M. Holmström, H. Nilsson, Y. Futaana, R. Ramstad, M. Yamauchi, E. Dubinin, and M. Fraenz (2013), Solar cycle effects on the ion escape from Mars, *Geophys. Res. Lett.*, *40*, 6028–6032, doi:10.1002/2013GL058154.

Ma, Y., A. F. Nagy, I. V. Sokolov, and K. C. Hansen (2004), Three-dimensional, multispecies, high spatial resolution MHD studies of the solar wind interaction with Mars, *J. Geophys. Res.*, *109*, A07211, doi:10.1029/2003JA010367.

Ma, Y., X. Fang, C. T. Russell, A. F. Nagy, G. Toth, J. G. Luhmann, D. A. Brain, and C. Dong (2014), Effects of crustal field rotation on the solar wind plasma interaction with Mars, *Geophys. Res. Lett.*, *41*, 6563–6569, doi:10.1002/2014GL060785.

Ma, Y. J., X. Fang, A. F. Nagy, C. T. Russell, and G. Toth (2014), Martian ionospheric responses to dynamic pressure enhancements in the solar wind, *J. Geophys. Res. Space Physics*, *119*, 1272–1286, doi:10.1002/2013JA019402.

Mahaffy, P. R., et al. (2014), The neutral gas and ion mass spectrometer on the Mars Atmosphere and Volatile Evolution mission, *Space Sci. Rev.*, doi:10.1007/s11214-014-0091-1.

McFadden, J., et al. (2015), The MAVEN 414 Suprathermal and thermal Ion Composition (STATIC) instrument, *Space Sci. Rev.*

Nagy, A., et al. (2004), The plasma environment of Mars, *Space Sci. Rev.*, *111*, 33–114.

Powell, K. G., P. L. Roe, T. J. Linde, T. I. Gombosi, and D. L. DeZeeuw (1999), A solution- adaptive upwind scheme for ideal magnetohydrodynamics, *J. Comput. Phys.*, *154*, 284–309.

Smith, F. L., and C. Smith (1972), Numerical evaluation of Chapman's grazing incidence integral Ch(χ, x), *J. Geophys. Res.*, *77*(19), 3592–3597, doi:10.1029/JA077i019p03592.

Toth, G., et al. (2012), Adaptive numerical algorithms in space weather modeling, *J. Comput. Phys.*, *231*(3), 870–903, doi:10.1016/j.jcp.2011.02.006.

Withers, P. (2009), A review of observed variability in the dayside ionosphere of Mars, *Adv. Space Res.*, *44*, 277–307.

Withers, P., M. O. Fillingim, R. J. Lillis, B. Häusler, D. P. Hinson, G. L. Tyler, M. Pätzold, K. Peter, S. Tellmann, and O. Witasse (2012), Observations of the nightside ionosphere of Mars by the Mars Express Radio Science Experiment (MaRS), *J. Geophys. Res.*, *117*, A12307, doi:10.1029/2012JA018185.